universe

MDPI

Article

Scaling Properties of Two-Particle–Two-Hole Responses in Asymmetric Nuclei for Neutrino Scattering Within the Relativistic Mean-Field Framework

Victor L. Martinez-Consentino [1,2,*], Jose E. Amaro [3,4] and Jorge Segovia [2]

[1] Departamento de Ciencias Integradas, Universidad de Huelva, E-21071 Huelva, Spain
[2] Departamento de Sistemas Físicos, Químicos y Naturales, Universidad Pablo de Olavide, E-41013 Sevilla, Spain; jsegovia@upo.es
[3] Departamento de Física Atómica, Molecular y Nuclear, 18071 Granada, Spain; amaro@ugr.es
[4] Instituto Carlos I de Física Teórica y Computacional, Universidad de Granada, 18071 Granada, Spain
* Correspondence: victormc@ugr.es

Abstract

We perform a systematic analysis of the nuclear dependence of two-particle–two-hole meson-exchange current contributions to inclusive lepton-nucleus scattering within the relativistic mean-field framework. We present microscopic calculations of nuclear responses for a set of 17 nuclei, ranging from helium to uranium, using a model with different Fermi momenta for protons and neutrons. We propose a novel scaling prescription based on the two-particle phase space and key nuclear parameters. The resulting description is accurate over a wide range of nuclear targets, with typical deviations below 10%, and allows for a separate treatment of the different emission channels. In addition, a consistent benchmark against electron-scattering data is provided. The parametrization presented provides a practical framework for extending the responses to different nuclear targets in neutrino event generators.

Keywords: neutrino scattering; electron scattering; meson-exchange currents; two-particle–two-hole; relativistic mean field; nuclear scaling

1. Introduction

The new era of neutrino experiments is characterized by an unprecedented technological leap. On the one hand, the sophisticated liquid-argon time projection chamber (LArTPC) technology dominates promising projects such as DUNE [1,2] and the Short-Baseline Neutrino (SBN) program, which includes experiments such as MicroBooNE, SBND, and ICARUS [3–5], establishing ^{40}Ar as a key nuclear target for present and future measurements. On the other hand, this experimental landscape is complemented by large-scale detectors such as Hyper-Kamiokande [6], based on water, and JUNO [7], whose goal is to improve the precision of neutrino measurements using hydrocarbon targets.

Although the field has historically relied on carbon or oxygen as theoretical reference nuclei for nuclear modeling, the current experimental program, driven by argon-based detectors and the multi-target strategy of MINERνA [8], requires going beyond this simplified framework. As neutrino interactions at the GeV scale are explored in neutron-rich media, the assumption that heavy nuclei can be described as simple scaled versions of symmetric nuclei [9–11] becomes increasingly questionable. This limitation is particularly

Check for updates

Academic Editor: Guillermo D. Megias

Received: 29 January 2026
Revised: 16 February 2026
Accepted: 18 February 2026
Published: 20 February 2026

https://doi.org/10.3390/universe12020056

evident in the so-called "dip region", located between the quasielastic (QE) peak and the $\Delta(1232)$ resonance.

In this kinematic regime, the cross-section is dominated by two-particle–two-hole excitations induced by meson-exchange currents (2p2h-MEC). A variety of theoretical approaches have been developed to describe these mechanisms with increasing sophistication [12–18], reflecting their crucial role in the reliable reconstruction of the incoming neutrino energy. However, as demonstrated in a recent study focused on nuclei with $A = 40$ [19], neglecting nuclear isospin asymmetry, as well as the use of the same Fermi momenta for protons and neutrons, leads to non-negligible deviations in the predicted nuclear response. These discrepancies increase further with increasing mass number.

The present work constitutes a natural continuation of that study [19] and addresses this issue through a systematic analysis of 2p2h responses across a broad set of nuclear targets. To this end, we extend microscopic calculations based on an asymmetric nuclear matter description within the Relativistic Mean Field (RMF) framework, previously applied to nuclei such as argon, calcium, and carbon [19–21], to an extensive set of seventeen nuclei. This set spans from light systems, such as lithium and helium, to heavy nuclei such as lead and uranium, thereby covering the full mass range relevant for neutrino scattering experiments and for inclusive electron scattering for which experimental data exist for a wide variety of nuclei [22,23].

The main objective of this study is to investigate scaling factors that allow for the prediction of the 2p2h response of an arbitrary nucleus starting from that of ^{12}C. In addition, we aim to characterize the nuclear dependence through the available two-particle phase space and nuclear parameters such as the number of nucleons, Fermi momenta, and the effective nuclear mass. The proposed formulation is grounded in a well-defined theoretical framework based on the factorization of the nuclear response and explicitly distinguishes both among different isotopes and among the various emission channels (pp, np, and nn). This strategy allows for a more controlled extrapolation from symmetric nuclei to neutron-rich systems, thereby mitigating the dependence on specific nuclear-model assumptions. To achieve this goal, the transverse response is described using a common functional form, with channel-dependent coefficients and phase-space factors, at fixed momentum transfer.

The paper is organized as follows. Section 2 summarizes the formalism for the treatment of asymmetric 2p2h-MEC responses within the RMF framework. In Section 3, the nuclear responses are scaled to ^{12}C, and the corresponding proportionality factors are extracted. Section 4 presents the factorized fitting strategy and the residual analysis. Finally, Section 5 summarizes the main conclusions of this study and outlines future perspectives.

2. The 2p2h-MEC Formalism

The inclusive lepton-nucleus scattering cross-section is obtained from the contraction of the leptonic tensor with the nuclear hadronic tensor $W^{\mu\nu}$, which encodes the nuclear dynamics. In addition to one-body processes, further contributions arise from 2p2h excitations induced by two-body electroweak currents. In these mechanisms, the exchanged boson interacts with a pair of nucleons, leading to the emission of two nucleons from the nucleus, as schematically illustrated in Figure 1.

In this work, we follow the formalism introduced in Ref. [19] for asymmetric nuclei, where protons and neutrons are treated independently by assigning different Fermi momenta, k_{Fp} and k_{Fn}. Within this framework, the contribution to the hadronic tensor associated with a given two-nucleon emission channel, corresponding to the nucleonic transition $N_1 N_2 \to N_1' N_2'$, can be written as

https://doi.org/10.3390/universe12020056

$$
\begin{aligned}
W^{\mu\nu}_{N_1'N_2'} = &\frac{V}{(2\pi)^9} \int d^3h_1\, d^3h_2\, d^3p_1'\, d^3p_2'\, \frac{(m_N^*)^4}{E_1 E_2 E_1' E_2'}\, w^{\mu\nu}_{N_1'N_2'}(\mathbf{p}_1', \mathbf{p}_2', \mathbf{h}_1, \mathbf{h}_2) \\
&\times \Theta_{N_1',N_1}(p_1', h_1)\, \Theta_{N_2',N_2}(p_2', h_2)\, \delta(E_1' + E_2' - E_1 - E_2 - \omega)\, \delta(\mathbf{p}_1' + \mathbf{p}_2' - \mathbf{h}_1 - \mathbf{h}_2 - \mathbf{q}), \qquad (1)
\end{aligned}
$$

where $\mathbf{h}_i$ ($\mathbf{p}_i'$) and E_i (E_i') denote the momenta and energies of the initial (final) nucleons, with effective mass m_N^*, and V is the volume. The delta functions enforce energy and momentum conservation, with ω and $\mathbf{q}$ denoting the energy and momentum transfer, respectively. The step functions $\Theta_{N',N}(p', h)$ restrict the phase space to occupied hole states below the corresponding Fermi momentum and to unoccupied particle states above it, for each isospin species. The elementary two-body tensor, $w^{\mu\nu}_{N_1'N_2'}$, is constructed from antisymmetrized two-body current matrix elements as

$$
w^{\mu\nu}_{N_1'N_2'} = G_s \sum_{s_1, s_2, s_1', s_2'} j_A^{\mu}(1', 2', 1, 2)^*\, j_A^{\nu}(1', 2', 1, 2), \qquad (2)
$$

where the sum runs over the spin projections of the initial (s_i) and final (s_i') nucleons. The two-body currents j_A^{μ} include pion-exchange mechanisms (seagull and pion-in-flight), as well as Δ excitation(Δ-forward and Δ-backward). Their explicit expressions are given in Ref. [20]. The factor G_s accounts for the symmetry of the initial/final state, and prevents double counting in channels involving identical nucleons. For inclusive neutrino-induced reactions, the factor takes the value $G_s = 1/2$. For electron-induced reactions, $G_s = 1/4$ in the symmetric pp and nn channels, while $G_s = 1$ in the asymmetric np channel.

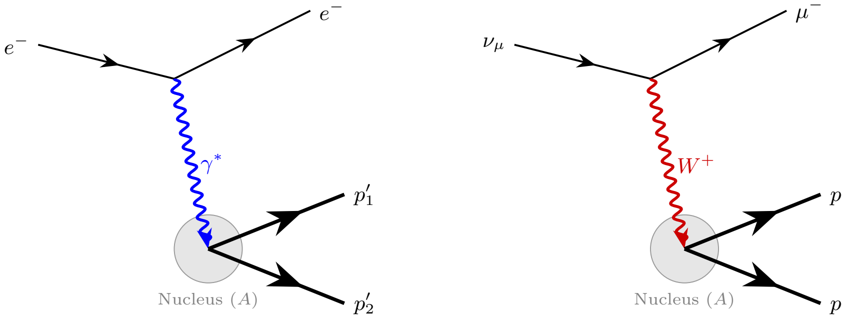

(a) Electron Scattering **(b) Neutrino Scattering**

Figure 1. Schematic representation of two-particle emission in lepton-nucleus scattering: electron scattering mediated by the exchange of a virtual photon (**a**) and neutrino scattering mediated by the exchange of a charged W^+ boson (**b**).

Medium effects are incorporated through an effective description inspired by relativistic mean-field models of nuclear matter [24]. Within this approach, nucleons propagate with modified single-particle properties that effectively encode the action of scalar and vector mean fields in the nuclear medium. The medium modification is introduced through effective masses for the nucleon and the $\Delta(1232)$ resonance:

$$
m_N^* = m_N - g_s \phi_0, \qquad m_\Delta^* = m_\Delta - g_s^\Delta \phi_0. \qquad (3)
$$

Here, g_s and g_s^Δ are effective scalar couplings and ϕ_0 denotes the mean-field expectation value of the scalar field. For observables that depend only on energy differences between initial and final nucleon states, such as the quasielastic 1p-1h response and the seagull and pion-in-flight 2p2h mechanisms, the contribution of the vector mean field cancels explicitly. In contrast, mechanisms involving an intermediate Δ excitation depend on absolute energies, so that the vector mean field shifts the Δ pole and modifies both the strength and the shape of the corresponding response.

For simplicity, a universal coupling is assumed [25], assigning the same vectorial energy to both nucleons and the Δ resonance, $E_v^N = E_v^\Delta$. The effective nucleon and Δ masses, together with the proton and neutron Fermi momenta employed for each nucleus, are summarized in Table 1.

These parameters (k_{Fp}, k_{Fn}, m_N^*, and m_Δ^*) are determined through a phenomenological fit to more than 20,000 data points of inclusive electron-nucleus scattering available in the Quasielastic Electron Nucleus Scattering Archive of the University of Virginia [22,23]. The resulting values have been further validated against recent high-precision measurements from JLab [26] and MAMI [27]. The parameters listed in Table 1 are consistent with those obtained in previous Superscaling analyses [17,28], which employed a single effective Fermi momentum. In this work, we use independent Fermi momenta for protons (k_{Fp}) and neutrons (k_{Fn}) to account for nuclear asymmetry which is equivalent to the value taken in the previous references. In our procedure, the Fermi momentum and the nucleon effective mass are varied to best describe the quasielastic peak in kinematics where the peak is clearly distinguishable (excluding regions of very high or low momentum transfer). Subsequently, the effective Δ mass m_Δ^* is adjusted to reproduce the Δ-resonance maximum, ensuring the peak position remains consistent with Relativistic Fermi Gas predictions [17].

Table 1. Nuclear parameters employed: proton and neutron numbers, effective nucleon and Δ masses normalized, and proton and neutron Fermi momenta (in MeV/c).

Nucleus	Z	N	m_N^*/m_N	m_Δ^*/m_Δ	k_{Fp}	k_{Fn}
^{4}He	2	2	0.90	0.922	160	160
^{6}Li	3	3	0.80	0.846	165	165
^{9}Be	4	5	0.80	0.846	190	205
^{12}C	6	6	0.80	0.846	225	225
^{16}O	8	8	0.80	0.846	230	230
^{24}Mg	12	12	0.75	0.807	235	235
^{27}Al	13	14	0.80	0.846	235	240
^{40}Ar	18	22	0.73	0.792	237	256
^{40}Ca	20	20	0.73	0.792	240	240
^{48}Ca	20	28	0.73	0.792	240	268
^{56}Fe	26	30	0.70	0.770	236	248
^{59}Ni	28	31	0.67	0.747	234	242
^{89}Y	39	50	0.65	0.732	232	252
^{119}Sn	50	69	0.65	0.732	230	256
^{181}Ta	73	108	0.65	0.732	228	260
^{208}Pb	82	126	0.65	0.732	230	265
^{238}U	92	146	0.65	0.732	252	293

Following the integration procedure described in Ref. [29], momentum conservation is used to perform the integration over $\mathbf{p}'_2$, and rotational invariance around the direction of the momentum transfer is exploited. The resulting nuclear response functions can be expressed as

$$\begin{aligned} R^K_{N'_1 N'_2} &= \frac{V}{(2\pi)^9} \int d^3p'_1\, d^3h_1\, d^3h_2\, \frac{(m_N^*)^4}{E_1 E_2 E'_1 E'_2}\, r^K(\mathbf{p}'_1, \mathbf{p}'_2, \mathbf{h}_1, \mathbf{h}_2) \\ &\times \Theta_{N'_1,N_1}(p'_1, h_1)\, \Theta_{N'_2,N_2}(p'_2, h_2)\, \delta(E'_1 + E'_2 - E_1 - E_2 - \omega), \end{aligned} \tag{4}$$

where K labels the different response channels and r^K denotes the corresponding reduced response function. The integration over the energy-conserving Dirac delta is performed in the center-of-mass system. For electromagnetic interactions, only the longitudinal and transverse responses contribute:

$$R^{L}_{\rm em} = W^{00}_{\rm em}, \qquad R^{T}_{\rm em} = W^{11}_{\rm em} + W^{22}_{\rm em}, \tag{5}$$

with allowed final-state channels pp, np, and nn. For charged-current neutrino reactions, five independent response functions contribute:

$$\begin{aligned} R^{CC} = W^{00}, \quad R^{CL} = -\tfrac{1}{2}(W^{03} + W^{30}), \quad R^{LL} = W^{33}, \\ R^{T} = W^{11} + W^{22}, \quad R^{T'} = -\tfrac{i}{2}(W^{12} - W^{21}), \end{aligned} \tag{6}$$

3. Scaling of 2p2h Responses Relative to Carbon

We compute the 2p2h nuclear response functions for a set of seventeen nuclei at a fixed momentum transfer $q = 500$ MeV$/c$, corresponding to a kinematic region where the nuclear response is close to its maximum and which is relevant for modern neutrino experiments. For each nuclear target X and response channel K, we define the 2p2h scaling ratio relative to ^{12}C as

$$\mathcal{R}^{K}_{N_1'N_2'}(X;\omega) \equiv \frac{R^{K}_{N_1'N_2'}(X; q = 500, \omega)}{R^{K}_{N_1'N_2'}(^{12}\text{C}; q = 500, \omega)} \approx \text{const.} \tag{7}$$

As discussed in Ref. [19], this ratio exhibits only a weak dependence on both the response channel K and the momentum transfer. In that reference, it is shown that the ratio evaluated at $q = 1000$ MeV$/c$ is very similar to that obtained at $q = 500$ MeV$/c$. This behavior is also consistent with other parametrizations available in the literature [9–11], where the scaling is found to be largely independent of both the momentum transfer and the specific response considered. Accordingly, in the present analysis we restrict ourselves to the transverse channel and drop the index K, so that the ratio is simply denoted as $\mathcal{R}$.

In practice, for each nucleus we extract a single effective scaling factor by evaluating the transverse responses R^{T} at their respective maxima and taking the ratio of peak values, dividing the maximum of the nucleus X by that of ^{12}C.

The peak positions occur at very similar energy transfers, ensuring a well-defined normalization. The scaling ratios are therefore evaluated by taking $\mathcal{R}$ at the maximum of the transverse response, which for $q = 500$ MeV$/c$ lies around $\omega \simeq 300$–400 MeV.

Figures 2 and 3 display the transverse 2p2h responses for neutrino-induced reactions in the $np \to pp$ and $nn \to np$ emission channels, respectively, for the seventeen nuclei considered. The ^{12}C result is shown as a dashed black curve, whereas the other nuclei are rescaled by dividing by their corresponding scaling factor $\mathcal{R}$, quoted in each subpanel.

All responses exhibit a pronounced peak as a function of ω, consistent with the leading role of Δ-driven MEC dynamics in this kinematic domain. In the $np \to pp$ channel (Figure 2), the rescaled curves show a good collapse around the carbon reference. The lightest nuclei (^{4}He, ^{6}Li, ^{9}Be) display small residual differences, including a mild shift of the peak region with respect to ^{12}C. Within the RMF-inspired effective description, variations in the effective nucleon and Δ masses and in the corresponding Fermi momenta induce small changes in the peak position and width, effects that are more visible in light systems.

Intermediate-mass nuclei provide the most stable behavior: oxygen, magnesium, and aluminum lie very close to the carbon reference over the peak region. This point matters for applications, since ^{40}Ar and ^{40}Ca also follow the same pattern around the maximum, supporting controlled extrapolations from carbon to argon-based detectors.

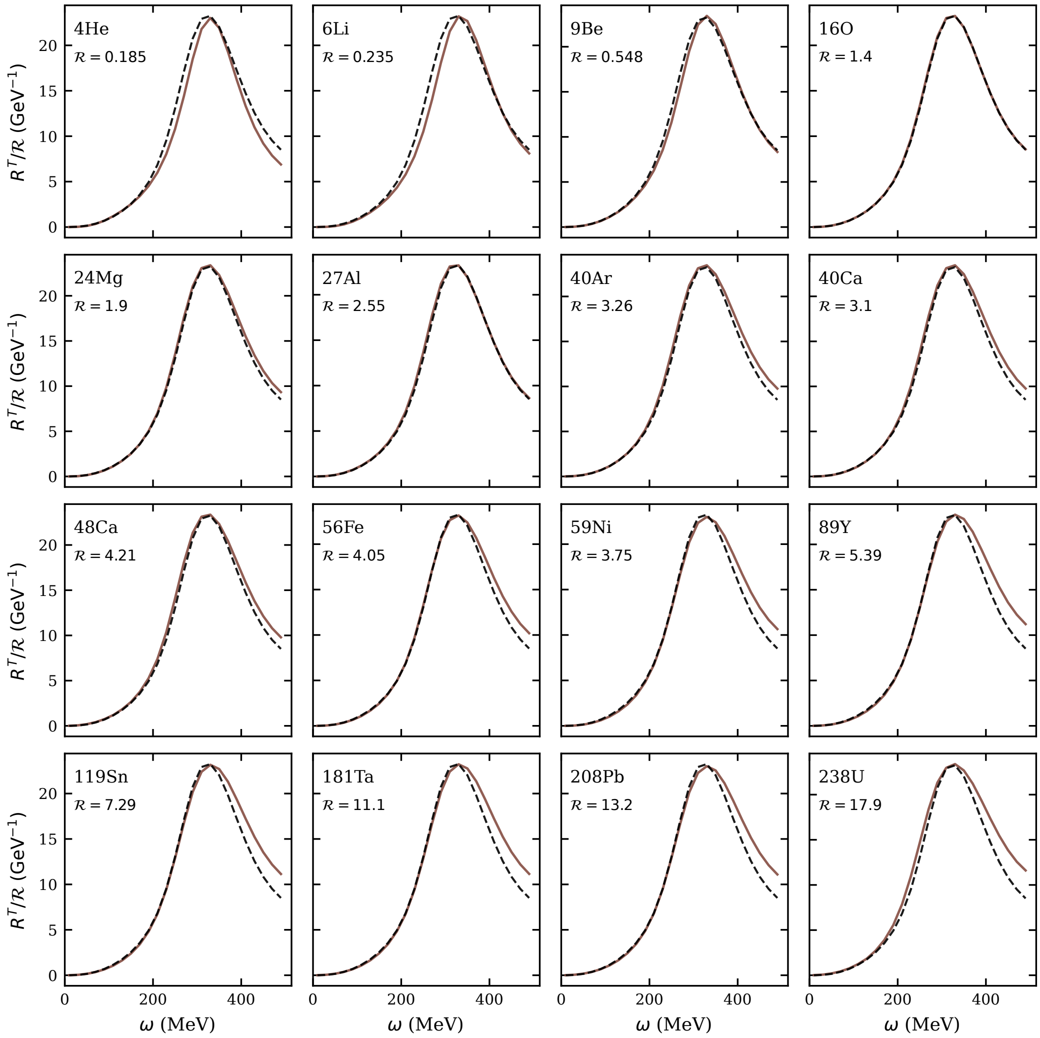

Figure 2. Transverse 2p2h responses for neutrino-induced $np \to pp$ emission at $q = 500$ MeV/c. Solid colored lines correspond to each nucleus, while the dashed black line shows the ^{12}C result. Each panel displays the response rescaled by the factor $\mathcal{R}$ indicated in the figure.

For heavy nuclei (tin, lead, uranium), the spread increases, especially at energy transfers above the Δ-peak maximum. Even so, the description remains adequate when one accounts for the strong growth of the absolute 2p2h strength with mass number.

In the $nn \to np$ channel (Figure 3), we find the same overall trend but with an absolute magnitude roughly six times smaller than in the $np \to pp$ channel. Here the scaling is visibly less accurate, consistent with the enhanced sensitivity of the $nn \to np$ response to neutron excess. The peak region is also broader and less sharply defined. This behavior follows from the interplay of Δ mechanisms: the Δ-forward diagram dominates channels with two protons in the final state, whereas the Δ-backward contribution becomes comparatively more relevant in the np final channel, producing an effective smearing in the ω dependence, in line with the analysis in Ref. [30]. In both channels, $\mathcal{R}$ increases generally with atomic number, tracking the approximate proportionality of the 2p2h strength to the nuclear volume. In Appendix A, we compare the corresponding transverse electromagnetic T responses for electron-induced reactions in the nn, np, and pp channels, using coefficients different from those employed for neutrinos.

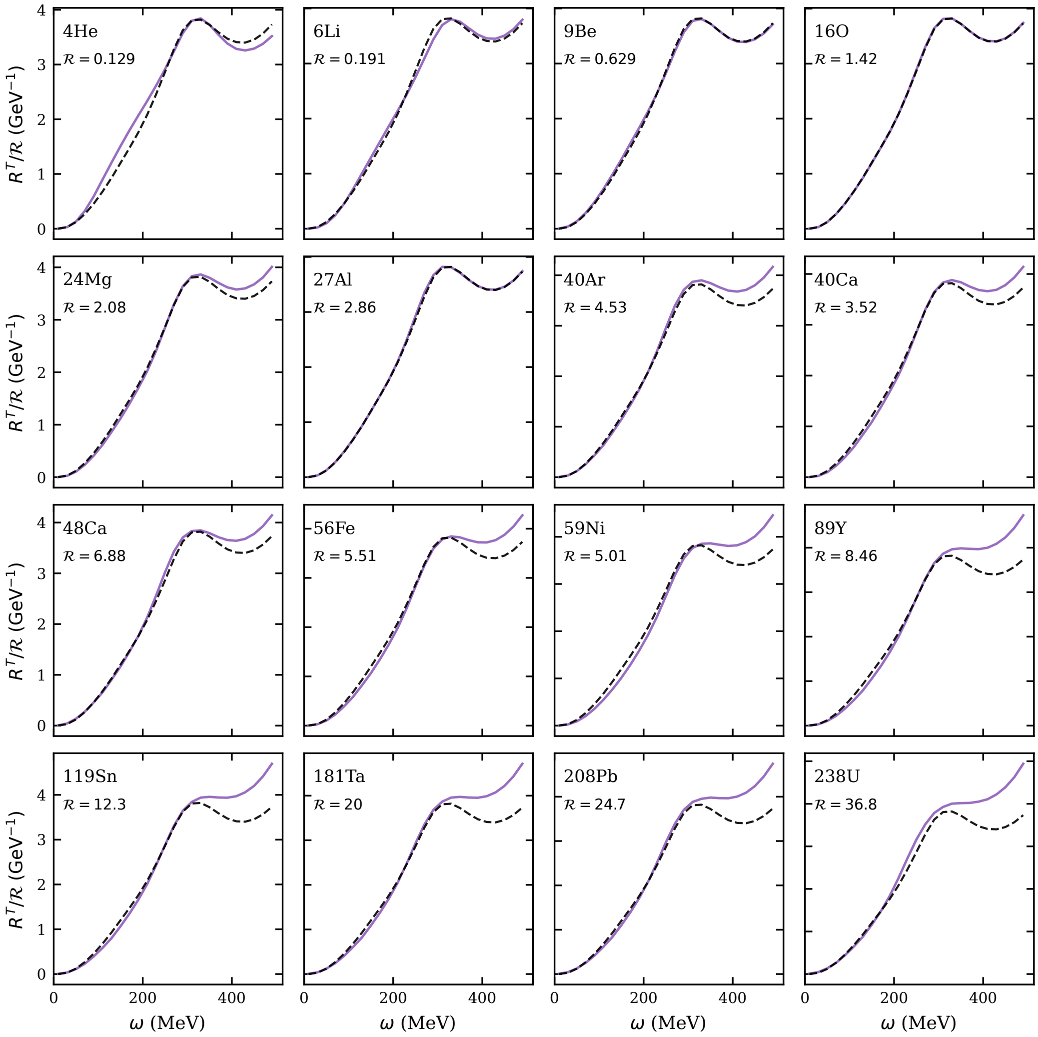

Figure 3. Same as Figure 2 but for neutrino-induced $nn \to np$ emission.

In Figures 4 and 5 we apply the same scaling analysis to the T' response in neutrino-induced reactions. The scaling factor is extracted from the T response and then used for the remaining neutrino responses (CC, CL, LL, and T'). In the energy range considered, T and T' dominate the neutrino cross-section. We also obtain the approximate factor $\sim 1/2$ between T and T', as reported in Ref. [31]. Overall, the rescaled T and T' responses follow the same pattern, with small channel-dependent differences. For example, in the pp final-state channel for ^{208}Pb the maximum ratio extracted from T' is slightly larger than the reference value.

Nevertheless, this analysis provides a useful test to assess whether the scaling behavior identified for the transverse channel also extends to other response functions. This aspect is particularly relevant in the antineutrino case, since the T' response changes sign, thereby reducing the cross-section and increasing the relative contribution of the other responses.

Table 2 summarizes the scaling ratios $\mathcal{R}$ for all nuclei and emission channels, normalized to unity for ^{12}C at $q = 500$ MeV$/c$. The ratios grow monotonically with nuclear mass, mirroring the strong increase in the overall 2p2h strength with nuclear size. For a fixed nucleus, channels involving nn pairs typically give the largest $\mathcal{R}$, followed by np, while pp channels show the weakest mass dependence. The fact that neutrino- and electron-induced reactions exhibit similar global trends supports the use of $\mathcal{R}$ as a stable, nucleus-dependent scaling factor.

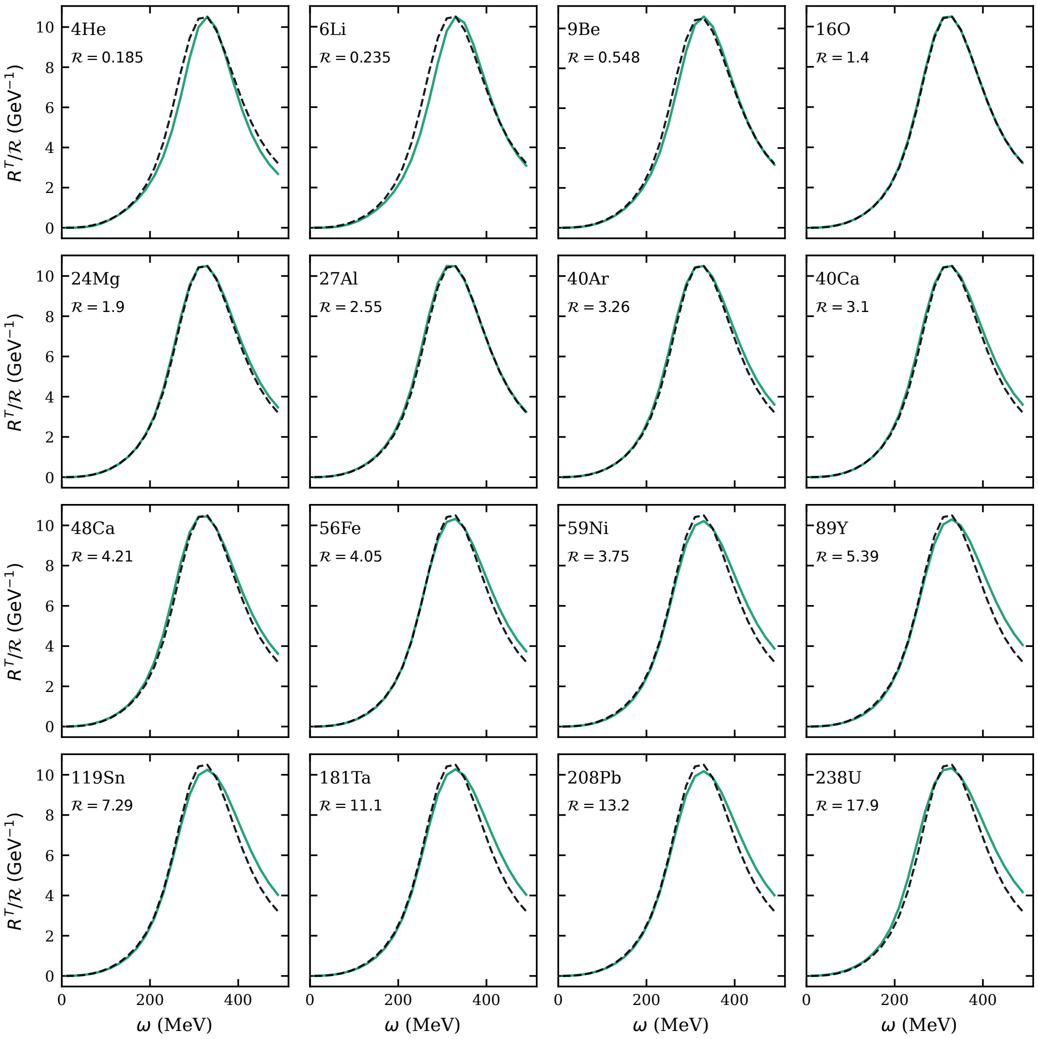

Figure 4. Response $R^{T'}$ rescaled to carbon for neutrino-induced $np \to pp$ emission at $q = 500$ MeV$/c$. Solid colored lines correspond to each nucleus, while the dashed black line shows the ^{12}C result. Each panel displays the response rescaled by the factor $\mathcal{R}$ indicated in the figure.

A striking feature is the much steeper mass dependence of the $\nu(np)$ and $e(nn)$ channels. From helium to uranium, these ratios increase by a factor of about 300, whereas the remaining channels grow by ∼100–120. This trend is quantified by the scaling ratios reported in Table 2, which span more than an order of magnitude across the nuclear chart. For example, in the neutrino-induced $np \to pp$ channel the ratio increases from $\mathcal{R} \simeq 0.185$ for ^{4}He to $\mathcal{R} \simeq 17.9$ for ^{238}U, whereas in the $nn \to np$ channel it reaches $\mathcal{R} \simeq 36.8$ for ^{238}U (all values normalized to unity for ^{12}C).

Figure 6 collects all transverse responses rescaled to ^{12}C for both neutrino and electron reactions. After applying the inverse factors $1/\mathcal{R}$, the results for all nuclei fall within a narrow band around the carbon reference, showing that the leading nuclear dependence can be factorized to a good approximation. The collapse is tight on the low-ω side and near the Δ peak, where the dominant 2p2h strength is concentrated, while a larger spread appears at higher energy transfer, where some nuclei do not scale as well. The np channel shows the largest residual deviations in both electron- and neutrino-induced cases, pointing to a stronger channel-specific nuclear dependence.

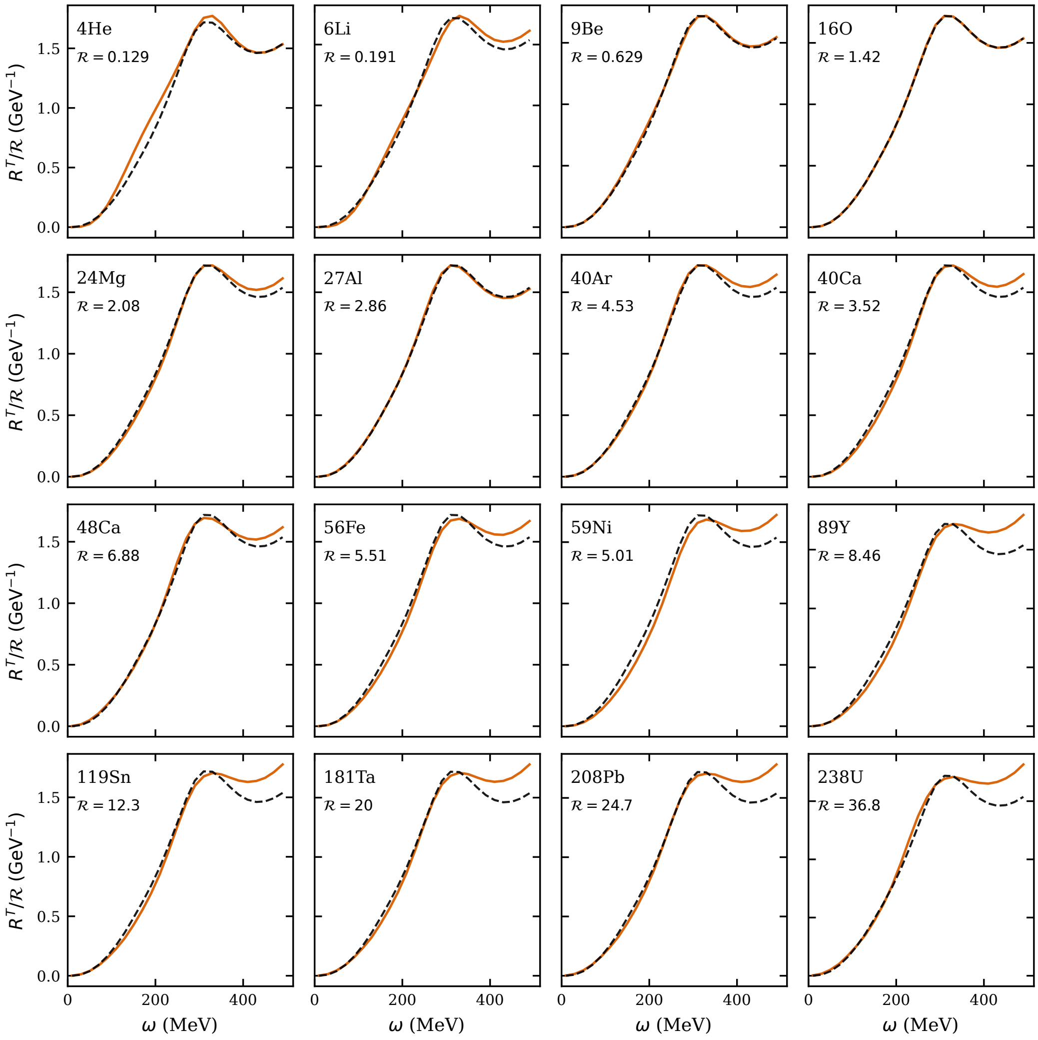

Figure 5. Same as Figure 4 but for neutrino-induced $nn \to np$ emission.

Table 2. Scaling ratios $\mathcal{R}$ for different nuclei and emission channels. The labels pp, np, and nn refer to the final-state nucleon pair. All values are normalized to unity for ^{12}C at $q = 500$ MeV$/c$.

Nucleus	$\nu(pp)$	$\nu(np)$	$e(pp)$	$e(np)$	$e(nn)$
^{4}He	0.185	0.129	0.117	0.181	0.117
^{6}Li	0.235	0.191	0.160	0.234	0.160
^{9}Be	0.518	0.629	0.364	0.547	0.597
^{12}C	1.000	1.000	1.000	1.000	1.000
^{16}O	1.399	1.422	1.437	1.399	1.437
^{24}Mg	1.901	2.075	2.062	1.931	2.062
^{27}Al	2.547	2.859	2.507	2.537	2.928
^{40}Ar	3.257	4.530	3.012	3.279	4.566
^{40}Ca	3.096	3.521	3.484	3.165	3.484
^{48}Ca	4.210	6.881	3.484	4.172	6.976
^{56}Fe	4.050	5.508	3.914	4.082	5.251
^{59}Ni	3.755	5.011	3.759	3.798	4.636
^{89}Y	5.389	8.457	4.772	5.482	7.874
^{119}Sn	7.288	12.32	5.950	7.331	11.39
^{181}Ta	11.10	20.03	8.442	11.12	18.65
^{208}Pb	13.24	24.73	9.758	13.07	23.22
^{238}U	17.90	36.79	14.48	17.76	35.95

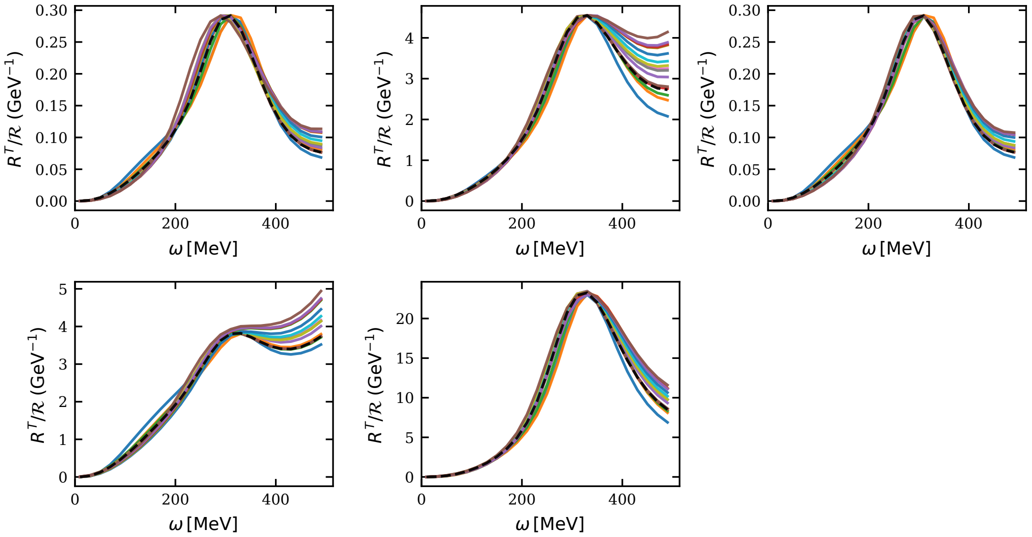

Figure 6. Transverse responses $R^T(X)$ rescaled to ^{12}C by dividing by the corresponding scaling ratio $\mathcal{R}$, for the seventeen nuclei considered at $q = 500$ MeV$/c$. The dashed black lines represent the results for ^{12}C, while the different colored lines correspond to the various rescaled nuclei considered in this work. (**top**) pp, np, and nn channels in electron scattering. (**bottom**) np (**left**) and pp (**right**) final-state channels in neutrino scattering.

We emphasize that this collapse does not imply exact scaling but rather a similar behavior of the rescaled responses across nuclei, with visible residual nuclear dependence that falls within the typical uncertainties associated with 2p2h responses.

4. Factorized Parametrization of the 2p2h Nuclear Response

In this section we introduce the factorized parametrization used to capture the nuclear dependence of the 2p2h responses. The input is the set of scaling ratios listed in Table 2, extracted from the microscopic RMF calculations at $q = 500$ MeV$/c$ and at the energy transfer corresponding to the maximum of the Δ peak, $\omega = \omega_\Delta^{\max}$.

Previous studies, such as Refs. [19,31,32], have shown that the scaling behavior of the 2p2h response can be partially interpreted in terms of a phase-space proportionality. While this approach provides a reasonable description for nuclei with similar mass numbers (e.g., ^{12}C and ^{40}Ca), significant deviations emerge for heavier systems such as lead or uranium, indicating that additional sources of nuclear dependence must be taken into account. Motivated by these observations, we decompose the nuclear response in Equation (4) within a factorized scheme of the form

$$R^K_{N_1'N_2'}(X;q,\omega) = V(X)\,F_{N_1N_2}(X;q,\omega)\,\frac{\langle r^K_{N_1'N_2'}(X;q,\omega)\rangle}{(2\pi)^9}\,, \tag{8}$$

It is important to emphasize that Equation (8) does not introduce any approximation. It follows exactly from the definition of the averaged reduced response $\langle r\rangle$. This factorized form isolates a volume-like contribution $V(X)$, a reduced phase-space factor $F_{N_1N_2}(X)$, and an averaged reduced single-pair response $r^K_{N_1'N_2'}(X)$, which contains the remaining dynamical and many-body nuclear dependence. We define the scaling ratio relative to ^{12}C as

$$\mathcal{R}(X) \equiv \frac{R^K_{N_1'N_2'}(X)}{R^K_{N_1'N_2'}(^{12}\mathrm{C})} = \nu(X)\,\varphi_{N_1N_2}(X)\,\rho(X)\,, \tag{9}$$

with

$$\nu(X) \equiv \frac{V(X)}{V(^{12}\text{C})}, \qquad \varphi_{N_1N_2}(X) \equiv \frac{F_{N_1N_2}(X)}{F_{N_1N_2}(^{12}\text{C})}, \qquad \rho(X) \equiv \frac{r^K_{N_1'N_2'}(X)}{r^K_{N_1'N_2'}(^{12}\text{C})}. \tag{10}$$

In our implementation, the volume-like factor entering the normalization is defined under the assumption that protons and neutrons occupy the same spatial volume within the nucleus. Within this picture, the proton and neutron densities differ through their respective Fermi momenta, but the geometric volume is taken to be common. Under this assumption, the volume factor can be written equivalently as

$$\frac{V(X)}{(2\pi)^3} = \frac{3\,Z}{8\pi\,k^3_{Fp}} = \frac{3\,N}{8\pi\,k^3_{Fn}}, \tag{11}$$

so that $\nu(X)$ is fully determined by Z (or by N), and the corresponding Fermi momentum.

The factor $F_{N_1N_2}(X)$ represents the 2p2h phase-space contribution with the volume term removed. Although it is formally defined as a seven-dimensional integral, it can be accurately approximated by an analytical expression obtained within the frozen approximation and by neglecting Pauli blocking effects, as discussed in Equations (39) and (40) of Ref. [33]. Within this approximation, the phase-space factor can be rewritten in the RMF framework allowing for different proton and neutron Fermi momenta as

$$F(q,\omega)_{N_1N_2} = 4\pi\left(\frac{4}{3}\pi k^3_{FN_1}\right)\left(\frac{4}{3}\pi k^3_{FN_2}\right)\frac{m^{*2}_N}{2}\,\frac{p''_1}{E''_1}, \tag{12}$$

where the ratio p''_1/E''_1 is given by

$$\frac{p''_1}{E''_1} = \sqrt{1 - \frac{4m^{*2}_N}{(2m^*_N+\omega)^2 - q^2}}. \tag{13}$$

This expression shows explicitly that the available two-particle phase space grows rapidly with increasing energy transfer ω and approaches a constant value in the asymptotic limit $\omega \to \infty$, leading to

$$F(q,\infty)_{N_1N_2} = 4\pi\left(\frac{4}{3}\pi k^3_{FN_1}\right)\left(\frac{4}{3}\pi k^3_{FN_2}\right)\frac{m^{*2}_N}{2}. \tag{14}$$

In the present implementation, we factor out only the leading dependence on the proton and neutron Fermi momenta. Any remaining kinematic and dynamical dependence either cancels explicitly when forming the scaling ratio or is retained in the reduced response. One example of the latter is the effective nucleon mass, which also enters the phase-space structure and whose contribution is ultimately absorbed into the reduced-response scaling function $\rho(X)$. Accordingly, the phase-space term that we factorize for each emission channel is taken to be

$$F_{np} \propto k^3_{Fp}\,k^3_{Fn}, \qquad F_{pp} \propto k^6_{Fp}, \qquad F_{nn} \propto k^6_{Fn}, \tag{15}$$

While the volume and phase-space factors can be computed using analytical expressions, the reduced response involves a much more complex dynamical structure. For this reason, all the remaining nuclear dependence is collected in the reduced-response scaling function term $\rho(X)$. We model $\rho(X)$ with an ansatz that encodes (i) proton–neutron imbalance through the Fermi momenta k_{Fp} and k_{Fn}, and (ii) RMF medium effects through the nucleon effective mass. Note that, once the leading volume dependence has been factored out, the only quantities that vary from nucleus to nucleus in this model are the proton and neutron Fermi momenta and the effective mass. Accordingly, we parametrize $\rho(X)$ as

$$\rho(X) = 1 + b_1\left(\frac{k_{Fp}(X)}{k_{Fp}(^{12}C)} - 1\right) + b_2\left(\frac{k_{Fn}(X)}{k_{Fn}(^{12}C)} - 1\right) + b_3\left(\frac{m_N^*(X)}{m_N^*(^{12}C)} - 1\right), \tag{16}$$

The parametrization consists of three terms. The first term is dependent on the proton content of the nucleus by the proton Fermi momentum, the second term is proportional to the neutron Fermi momentum, and the third term accounts for effective-mass effects arising from the RMF framework. In a simple Fermi gas model, this last contribution, associated with the coefficient b_3, would not be required.

We use ^{12}C as the reference nucleus, fixing $k_{Fp}(^{12}\mathrm{C}) = k_{Fn}(^{12}\mathrm{C}) = 225\ \mathrm{MeV}/c$ and $m^*(^{12}\mathrm{C})/m_N = 0.8$. We also remark that the effective Δ mass, m^*_Δ, reported in Table 1, is an input of the microscopic RMF calculation and is not treated as an independent scaling variable. Its nuclear dependence is assumed to follow the same scaling behavior as the effective nucleon mass.

The fitted coefficients reported in Table 3 exhibit a clear dependence on the emission channel, reflecting the different dynamical mechanisms that govern each reaction. The relative weight of the k_{Fp} and k_{Fn} terms varies across channels, effectively encoding the sensitivity to proton-neutron imbalance through the different evolution of the two Fermi momenta with nuclear number. The effective-mass coefficient b_3 contributes with the same sign and with a similar magnitude in all cases, highlighting the role of RMF medium effects.

Table 3. Parameters of the reduced-response scaling function $\rho(X)$ for the different emission channels. The last column reports the coefficient of determination R^2 of the linear regression.

Channel	b_1	b_2	b_3	R^2
$e + nn \to e + nn$	0.77	−0.09	1.84	0.95
$e + np \to e + np$	−0.58	−0.20	1.95	0.99
$e + pp \to e + pp$	0.90	−0.20	1.78	0.97
$\nu_\mu + nn \to \mu + np$	0.43	−0.28	1.34	0.96
$\nu_\mu + np \to \mu + pp$	−0.64	−0.13	2.03	0.99

The values of R^2 (the coefficient of determination of the linear regression) reported in the table provide a global measure of the quality of the parametrization for each channel. The results demonstrate a uniformly high quality of the fit across all channels, with R^2 above 0.95. In Figure 7, we display the results of the separated channel fit as a function of the mass number A. We observe that, for all channels, the factor ρ tends to decrease with increasing nuclear size and approaches a nearly constant value for heavy nuclei. The figure also illustrates the relatively very good description in all channel. The pp channel, with $R^2 = 0.99$, is particularly relevant for neutrino-induced reactions, where it provides the dominant contribution.

It is important to emphasize, however, that the present parametrization is not intended to reproduce the microscopic 2p2h response of a specific nucleus-which is obtained from the underlying RMF calculations—but rather to describe how this response evolves across different nuclear targets over a wide mass range. To quantify the quality of the fit over this nuclear range, a quantitative validation is therefore performed through the analysis of the relative residuals shown in Figure 8, defined as

$$\delta(\%) = \frac{Y^{\mathrm{RMF}} - Y^{\mathrm{fit}}}{Y^{\mathrm{RMF}}} \times 100. \tag{17}$$

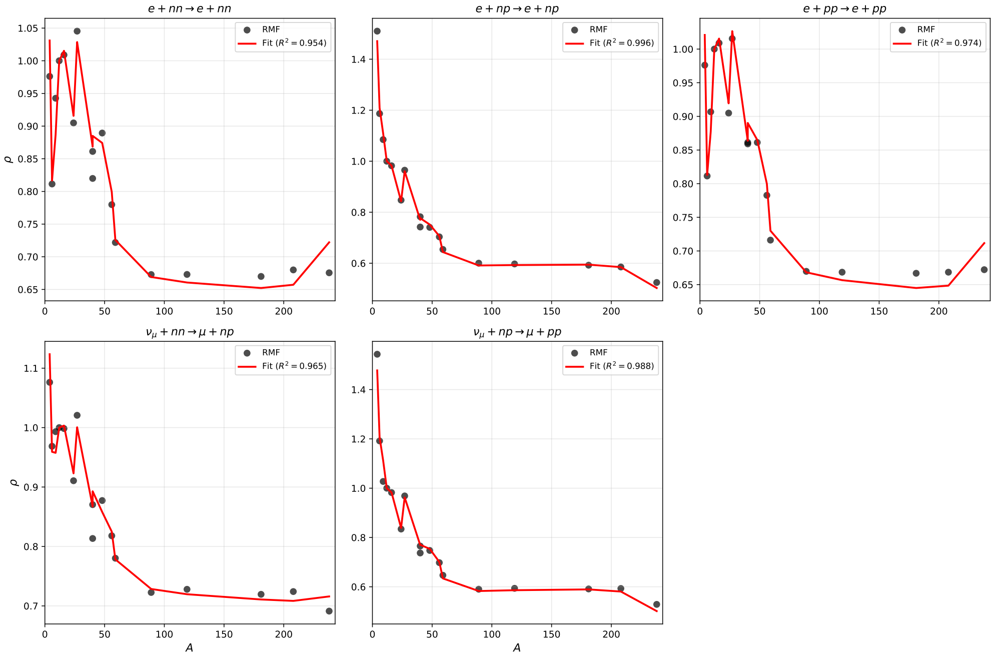

Figure 7. Comparison between the factorized fit (solid lines) and the microscopic RMF calculations as a function of the mass number A for the five emission channels considered. The fit is performed for $\rho(X)$ after dividing out the volume and reduced phase-space factors, see Equation (10).

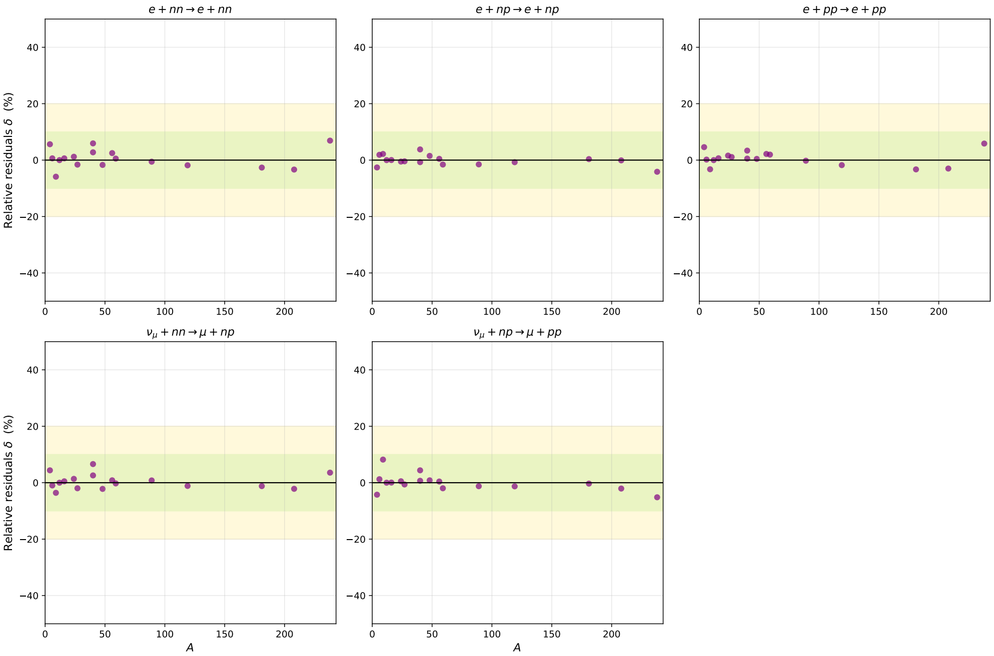

Figure 8. Relative residuals as a function of the mass number A for the five emission channels considered. The purple circles represent the different nuclei analyzed in this work. The green shaded area indicates a relative residual interval of ±10%, while the yellow shaded area corresponds to a ±20% relative residual interval.

The resulting parametrization reproduces the main trends in the scaling factors across different nuclei and emission channels. As shown by the residual analysis, the relative residuals remain typically within ±10%, corresponding to relative deviations of the order of 10%. As shown in Figure 8, the relative residuals display the largest dispersion for the lightest nuclei, where sizable positive and negative deviations are observed. For intermediate-mass systems, the residuals cluster more tightly around zero, with most values lying within the 5% band and exhibiting a smooth dependence on nuclear size. For the heaviest nuclei, the dispersion increases again, although it remains less pronounced than in the lightest systems and does not show a strong systematic bias.

5. Conclusions

In this work we investigated the nuclear dependence of two-particle–two-hole meson-exchange current contributions to inclusive electron–nucleus and neutrino-nucleus scattering within the relativistic mean-field framework, extending microscopic calculations from carbon to a broad set of nuclear targets ranging from light to heavy systems.

We find that the dominant nuclear dependence of the transverse two-particle responses can be largely absorbed into a nucleus-dependent scaling factor relative to carbon. For most medium-mass nuclei, the response shapes are similar in the vicinity of the peak, while departures from perfect scaling are mainly observed for the lightest and heaviest systems and at large energy transfers, where subleading nuclear effects become more relevant.

On the basis of these observations, we adopt a factorized form for the scaling ratio, separating volume and reduced phase-space contributions and collecting the remaining nuclear dependence in a reduced-response scaling function $\rho(X)$. We parametrize $\rho(X)$ using the proton and neutron Fermi momenta and the RMF effective mass, obtaining a compact representation of the microscopic results across nuclei rather than a statistical fit in the strict sense.

The overall quality of the parametrization is moderate, capturing the main trends in the scaling ratios across the nuclear chart. For medium-mass nuclei, the relative deviations are typically below the $\sim$10% level, as can be inferred from the residual analysis. Larger deviations are concentrated in the lightest and heaviest systems, reflecting both genuine nuclear-structure effects and the limitations imposed by the restricted set of microscopic calculations considered in this work, which spans 16 nuclei. These results illustrate that achieving a fully universal description across all nuclei and emission channels remains a challenging task within the present dataset.

Despite these limitations, the proposed scaling strategy provides a practical and transparent framework to extrapolate microscopic RMF calculations from a carbon reference to other nuclear targets of experimental interest, including neutron-rich nuclei. Its simplicity makes it well suited for exploratory implementations in neutrino event generators, where it can support a more controlled treatment of two-particle–two-hole contributions.

In future work, we plan to apply the same factorized scaling prescription to antineutrino-induced reactions. We will also explore comparisons with other microscopic 2p2h models, extend the set of benchmark nuclei, and confront the results with available experimental data. These steps will help to provide a more reliable and controlled input for neutrino oscillation experiments, in particular for analyses involving heavy targets.

Author Contributions: Author Contributions: Conceptualization, V.L.M.-C., J.E.A. and J.S.; methodology, V.L.M.-C., J.E.A. and J.S.; software, V.L.M.-C., J.E.A. and J.S.; validation, V.L.M.-C., J.E.A. and J.S.; formal analysis, V.L.M.-C., J.E.A. and J.S.; investigation, V.L.M.-C., J.E.A. and J.S.; resources, V.L.M.-C., J.E.A. and J.S.; data curation, V.L.M.-C., J.E.A. and J.S.; writing—original draft preparation, V.L.M.-C., J.E.A. and J.S.; writing—review and editing, V.L.M.-C., J.E.A. and J.S.; visualization, V.L.M.-C., J.E.A. and J.S.; supervision, V.L.M.-C., J.E.A. and J.S.; project administration, J.E.A. and J.S.; funding acquisition, J.E.A. and J.S. All authors have read and agreed to the published version of the manuscript.

Funding: This work was supported by Grant No. PID2023-147072NB-I00 funded by MICIU/AEI /10.13039/501100011033 and by the ERDF/EU, and by Grant No. FQM-225 funded by the Junta de Andalucía. Additional financial support was provided by the Spanish Ministry of Science, Innovation and Universities under Grant No. PID2022-140440NB-C22, and by the Junta de Andalucía under

Contracts PAIDI FQM-370 and PCI+D+i "Tecnologías avanzadas para la exploración del universo y sus componentes" (Code AST22-0001).

Data Availability Statement: The data are not publicly available. The data are available from the authors upon reasonable request.

Conflicts of Interest: The authors declare no conflicts of interest.

Abbreviations

The following abbreviations are used in this manuscript:

MEC	Meson-exchange currents
RMF	Relativistic mean field
CC	Charged-current
QE	Quasielastic
LArTPC	Liquid-argon time projection chamber
SBN	Short-Baseline Neutrino

Appendix A. Transverse Electromagnetic Response for the nn, np, and pp Channels

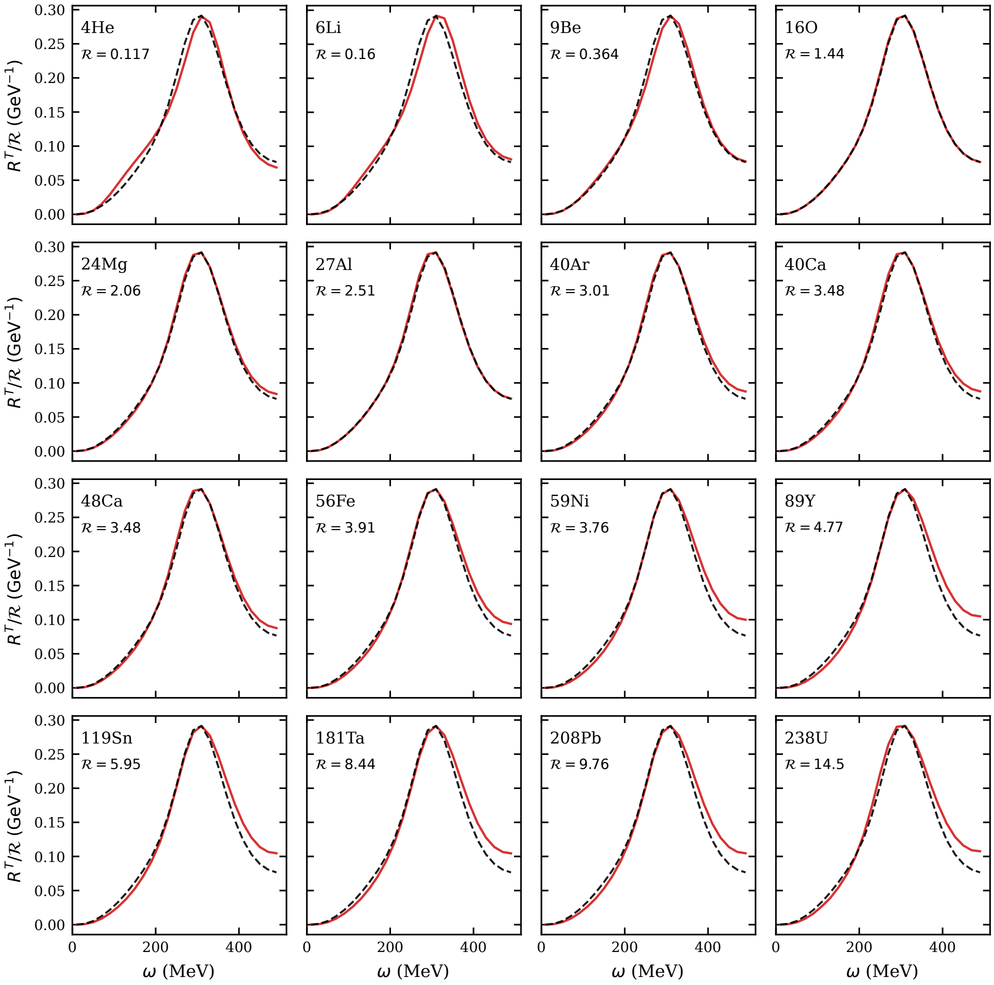

Figure A1. Transverse 2p2h responses for electron reaction $pp \to pp$ emission at $q = 500$ MeV$/c$. Solid colored lines correspond to each nucleus, while the dashed black line shows the ^{12}C result. Each panel displays the response rescaled by the factor $\mathcal{R}$ indicated in the figure.

In this appendix we present the transverse electromagnetic responses R^T_{em} and the corresponding scaling ratios for electron-induced reactions. These results are obtained using the same scaling procedure discussed in the main text, although they lead to ratios that differ from the neutrino case due to the different isospin structure of the electromagnetic and weak charged currents.

The analysis of the nn, np, and pp channels in electron scattering reveals systematic trends and allows for a direct comparison with neutrino-induced reactions. Figures A1, A2, and A3 display the transverse responses for the pp, np, and nn emission channels, respectively. In all cases, the same scaling prescription employed in the main analysis provides a satisfactory description for medium-mass nuclei. As in the neutrino case, larger deviations are observed for the lightest and heaviest systems, particularly at energy transfers above the peak.

It is worth noting that the scaling factors extracted for the electron-induced $nn \to nn$ channel exhibit both a magnitude and a growth with nuclear mass very similar to those found for the neutrino-induced $nn \to np$ channel. A comparable correspondence is also observed between the $np \to np$ channel in electron scattering and the $np \to pp$ channel in neutrino scattering. This does not imply that the scaling ratio $\mathcal{R}$ is solely determined by the isospin configuration of the initial nucleon pair but rather indicates that it also retains sensitivity to the detailed dynamics of each emission channel.

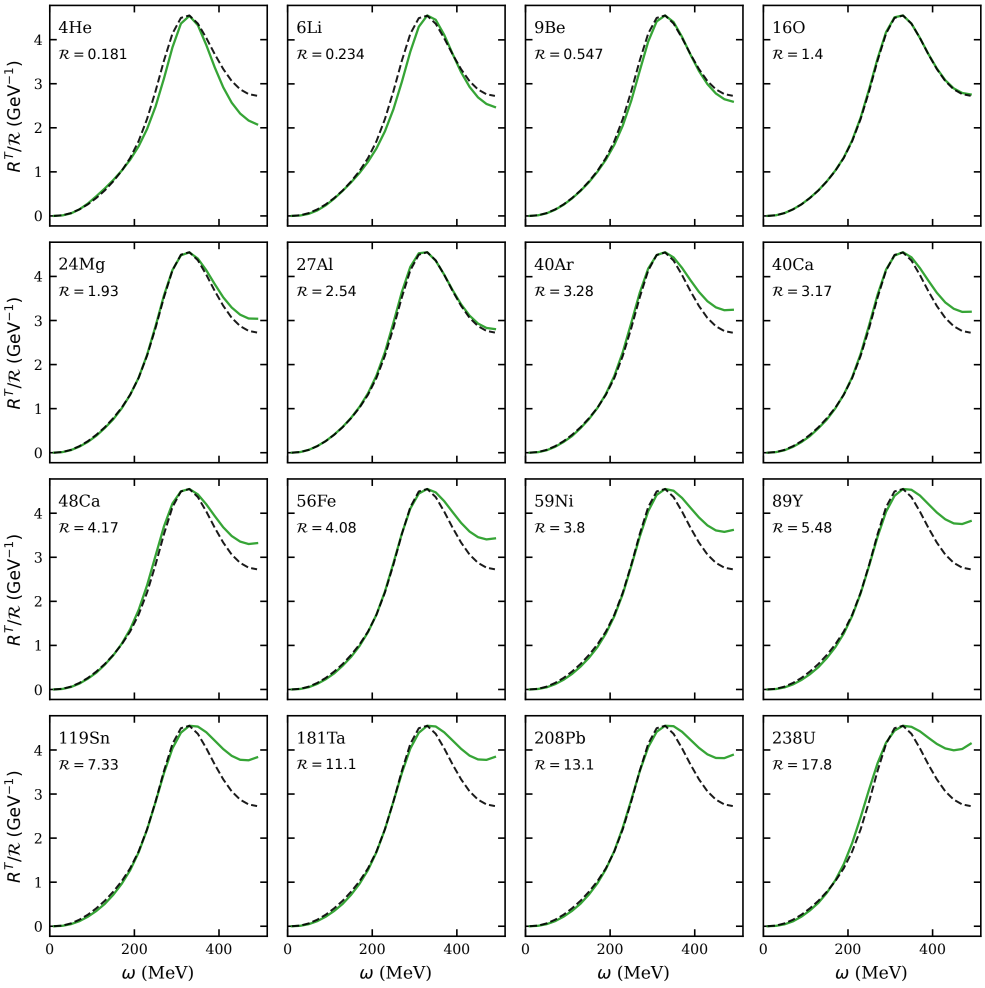

Figure A2. Same as Figure A1 but for $np \to np$ emission.

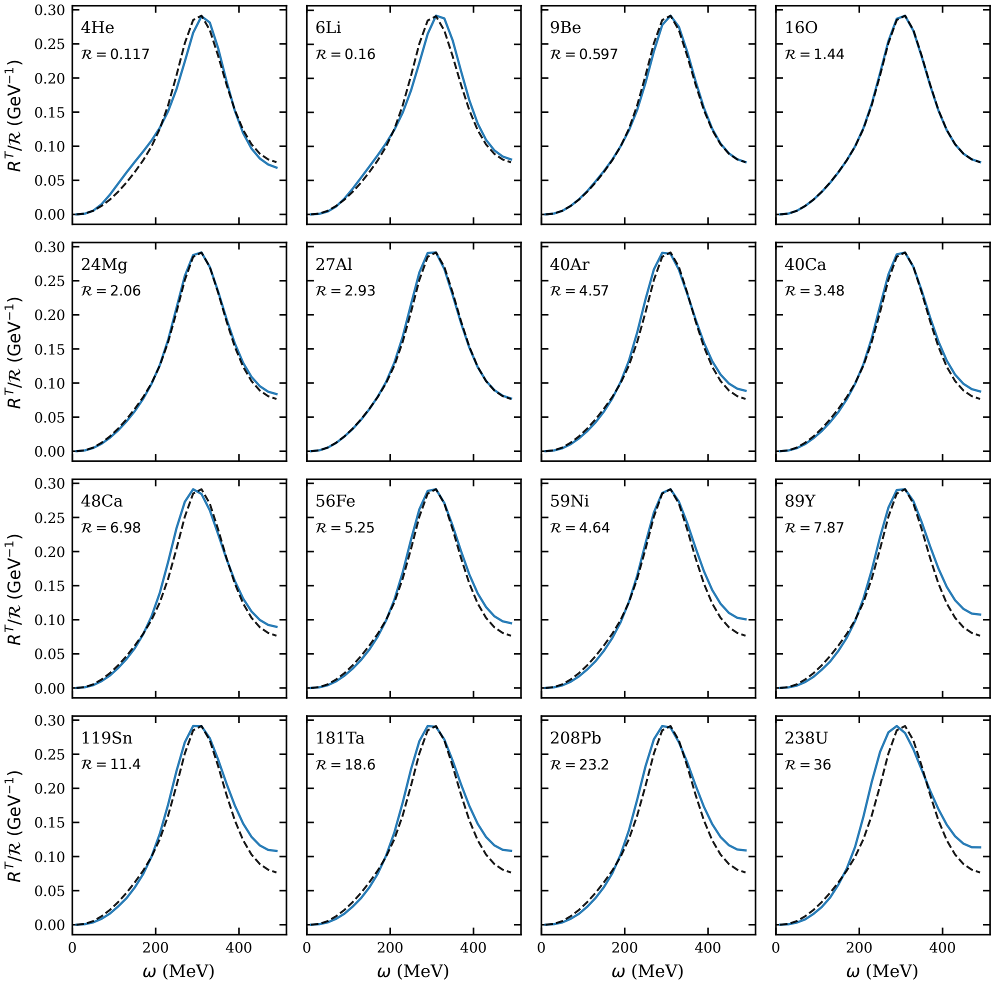

Figure A3. Same as Figure A1 but for $nn \to nn$ emission.

References

1. Abi, B.; Acciarri, R.; Acero, M.A.; Adamov, G.; Adams, D.; Adinolfi, M.; Ahmad, Z.; Ahmed, J.; Alion, T.; et al.; [DUNE Collaboration]. Deep Underground Neutrino Experiment (DUNE), Far Detector Technical Design Report, Volume I: Introduction to DUNE. *J. Instrum.* **2020**, *15*, T08008. [CrossRef]
2. Abi, B.; Acciarri, R.; Acero, M.A.; Adamov, G.; Adams, D.; Adinolfi, M.; Ahmad, Z.; Ahmed, J.; Alion, T.; et al.; [DUNE Collaboration]. Deep Underground Neutrino Experiment (DUNE), Far Detector Technical Design Report, Volume II: DUNE Physics. *arXiv* **2020**, arXiv:2002.03005. [CrossRef]
3. Abratenko, P.; Aduszkiewicz, A.; Akbar, F.; Artero Pons, M.; Asaadi, J.; Aslin, M.; Babicz, M.; Badgett, W.F.; Bagby, L.F.; et al.; [ICARUS Collaboration]. ICARUS at the Fermilab Short-Baseline Neutrino Program: Initial Operation. *Eur. Phys. J. C* **2023**, *83*, 467. [CrossRef] [PubMed]
4. Abratenko, P.; Andrade Aldana, D.; Arellano, L.; Asaadi, J.; Ashkenazi, A.; Balasubramanian, B.; Baller, B.; Barnard, A.; Barr, G.; [MicroBooNE Collaboration]. Measurement of Charged-Current Muon Neutrino–Argon Interactions Without Pions in the Final State Using the MicroBooNE Detector. *Phys. Rev. D* **2025**, *112*, 072007. [CrossRef]
5. Acciarri, R.; Adams, C.; Andreopoulos, C.; Asaadi, J.; Babicz, M.; Backhouse, C.; Badgett, W.; Bagby, L.F.; Barker, D.; et al.; [SBND Collaboration]. Construction of Precision Wire Readout Planes for the Short-Baseline Near Detector. *J. Instrum.* **2020**, *15*, P06033. [CrossRef]
6. Abe, K.; Abe, K.; Aihara, H.; Aimi, A.; Akutsu, R.; Andreopoulos, C.; Anghel, I.; Anthony, L.H.V.; Antonova, M.; et al.; [Hyper-Kamiokande Collaboration]. Hyper-Kamiokande Design Report. *arXiv* **2018**, arXiv:1805.04163. [CrossRef]
7. Abusleme, A.; Adam, T.; Ahmad, S.; Ahmed, R.; Aiello, S.; Akram, M.; An, F.; An, G.; An, Q.; et al.; [JUNO Collaboration]. JUNO Physics and Detector. *Prog. Part. Nucl. Phys.* **2022**, *123*, 103927. [CrossRef]
8. Aliaga, L.; Bagby, L.; Baldin, B.; Baumbaugh, A.; Bodek, A.; Bradford, R.; Brooks, W.K.; Boehnlein, D.; Boyd, S.; et al.; [MINERvA Collaboration]. Design, Calibration, and Performance of the MINERvA Detector. *Nucl. Instrum. Meth. A* **2014**, *743*, 130–159. [CrossRef]

9. Mosel, U.; Gallmeister, K. Mass dependence and isospin dependence of short-range correlated pairs. *Phys. Rev. C* **2016**, *94*, 034610. [CrossRef]
10. Dolan, S.; Megias, G.D.; Bolognesi, S. Implementation of the SuSAv2-meson exchange current 1p1h and 2p2h models in GENIE and analysis of nuclear effects in T2K measurements. *Phys. Rev. D* **2020**, *101*, 033003. [CrossRef]
11. Schwehr, J.; Cherdack, D.; Gran, R. GENIE implementation of IFIC Valencia model for QE-like 2p2h neutrino–nucleus cross section. *arXiv* **2016**, arXiv:1601.02038.
12. Nieves, J.; Ruiz Simo, I.; Vicente Vacas, M.J. Inclusive charged-current neutrino–nucleus reactions. *Phys. Rev. C* **2011**, *83*, 045501. [CrossRef]
13. Mosel, U.; Lalakulich, O.; Gallmeister, K. Energy Reconstruction in the Long-Baseline Neutrino Experiment. *Phys. Rev. Lett.* **2014**, *112*, 151802. [CrossRef] [PubMed]
14. Megias, G.D.; Amaro, J.E.; Barbaro, M.B.; Caballero, J.A.; Donnelly, T.W.; Ruiz Simo, I. Charged-current neutrino–nucleus reactions within the superscaling meson-exchange current approach. *Phys. Rev. D* **2016**, *94*, 093004. [CrossRef]
15. Van Cuyck, T.; Jachowicz, N.; González-Jiménez, R.; Ryckebusch, J.; Van Dessel, N. Seagull and pion-in-flight currents in neutrino-induced one- and two-nucleon knockout. *Phys. Rev. C* **2017**, *95*, 054611. [CrossRef]
16. Rocco, N.; Barbieri, C.; Benhar, O.; De Pace, A.; Lovato, A. Neutrino–nucleus cross section within the extended factorization scheme. *Phys. Rev. C* **2019**, *99*, 025502. [CrossRef]
17. Martinez-Consentino, V.L.; Ruiz Simo, I.; Amaro, J.E. Meson-exchange currents and superscaling analysis with relativistic effective mass of quasielastic electron scattering from ^{12}C. *Phys. Rev. C* **2021**, *104*, 025501. [CrossRef]
18. Russo, L.; Martini, M.; Dolan, S.; Munteanu, L.; Popov, B.; Giganti, C. Implementation of the Martini–Ericson–Chanfray–Marteau model in the GENIE neutrino event generator. *Phys. Rev. D* **2026**, *113*, 012006. [CrossRef]
19. Martinez-Consentino, V.L.; Segovia, J.; Amaro, J.E. Microscopic calculation of two-particle–two-hole meson-exchange currents in argon and asymmetric scaling properties for neutrino and electron scattering. *Phys. Rev. D* **2025**, *112*, 113011. [CrossRef]
20. Martinez-Consentino, V.L.; Amaro, J.E. Charged-current quasielastic neutrino scattering from ^{12}C in an extended superscaling model with two-nucleon emission. *Phys. Rev. D* **2023**, *108*, 113006. [CrossRef]
21. Barbaro, M.B.; Caballero, J.A.; De Pace, A.; Donnelly, T.W.; González-Jiménez, R.; Megias, G.D. Mean-field and two-body nuclear effects in inclusive electron scattering on argon, carbon, and titanium: The superscaling approach. *Phys. Rev. C* **2019**, *99*, 042501. [CrossRef]
22. Benhar, O.; Day, D.; Sick, I. An archive for quasielastic electron–nucleus scattering data. *arXiv* **2006**, arXiv:nucl-ex/0603032.
23. Benhar, O.; Day, D.; Sick, I. Inclusive quasielastic electron–nucleus scattering. *Rev. Mod. Phys.* **2008**, *80*, 189. [CrossRef]
24. Serot, B.D.; Walecka, J.D. *Advances in Nuclear Physics*; Negele, J.W., Vogt, E., Eds.; Plenum Press: New York, NY, USA, 1986; Volume 16.
25. Wehrberger, K. Electromagnetic response functions in quantum hadrodynamics. *Phys. Rep.* **1993**, *225*, 1–44. [CrossRef]
26. Murphy, M.; Dai, H.; Gu, L.; Abrams, D.; Ankowski, A.M.; Aljawrneh, B.; Alsalmi, S.; Bane, J.; Barcus, S.; Benhar, O. et al. [Jefferson Lab Hall A Collaboration]. Measurement of the cross sections for inclusive electron scattering in the E12-14-012 experiment at Jefferson Lab. *Phys. Rev. C* **2019**, *100*, 054606. [CrossRef]
27. Mihovilovič, M.; Doria, L.; Achenbach, P.; Ankowski, A.M.; Bacca, S.; Bosnar, D.; Denig, A.; Distler, M.O.; Esser, A.; Friščić, I.; et al. Measurement of the ^{12}C(e,e′) Cross Sections at $Q^2 = 0.8$ GeV$^2/c^2$. *Few-Body Syst.* **2024**, *65*, 78. [CrossRef]
28. Martinez-Consentino, V.L.; Ruiz Simo, I.; Amaro, J.E.; Ruiz Arriola, E. Fermi-momentum dependence of relativistic effective mass below saturation from superscaling of quasielastic electron scattering. *Phys. Rev. C* **2017**, *96*, 064612. [CrossRef]
29. Ruiz Simo, I.; Amaro, J.E.; Barbaro, M.B.; De Pace, A.; Caballero, J.A.; Donnelly, T.W. Relativistic model of 2p–2h meson-exchange currents in (anti)neutrino scattering. *J. Phys. G* **2017**, *44*, 065105. [CrossRef]
30. Martinez-Consentino, V.L.; Amaro, J.E. Exploring semi-inclusive two-nucleon emission in neutrino scattering: A factorized approximation approach. *Symmetry* **2024**, *16*, 247. [CrossRef]
31. Martinez-Consentino, V.L.; Amaro, J.E.; Ruiz Simo, I. Semiempirical formula for electroweak response functions in the two-nucleon emission channel in neutrino–nucleus scattering. *Phys. Rev. D* **2021**, *104*, 113006. [CrossRef]
32. Lalakulich, O.; Gallmeister, K.; Mosel, U. Many-body interactions of neutrinos with nuclei: Observables. *Phys. Rev. C* **2012**, *86*, 014614, Erratum in *Phys. Rev. C* **2014**, *90*, 029902. [CrossRef]
33. Ruiz Simo, I.; Albertus, C.; Amaro, J.E.; Barbaro, M.B.; Caballero, J.A.; Donnelly, T.W. Angular distribution in two-particle emission induced by neutrinos and electrons. *Phys. Rev. D* **2014**, *90*, 053010. [CrossRef]

https://doi.org/10.3390/universe12020056